Ultralong 1D Vacancy Channels for Rapid Atomic Migration during 2D Void Formation in Monolayer MoS$_2$

Qu Chen,[†,¶] Huashan Li,[‡,¶] Si Zhou,[†] Wenshuo Xu,[†] Jun Chen,[†] Hidetaka Sawada,[§] Christopher S. Allen,[†,∥] Angus I. Kirkland,[†,∥] Jeffrey C. Grossman,[⊥] and Jamie H. Warner*,[†]

[†]Department of Materials, University of Oxford, 16 Parks Road, Oxford OX1 3PH, United Kingdom

[‡]Sino-French Institute of Nuclear Engineering and Technology, Sun Yat-Sen University, Tang-Jia-Wan, Zhuhai City, Guangdong 519-082, P.R. China

[§]JEOL Ltd., 3-1-2 Musashino, Akishima, Tokyo 196-8558, Japan

[∥]Electron Physical Sciences Imaging Center, Diamond Light Source Ltd., Didcot, Oxfordshire OX11 0DE, United Kingdom

[⊥]Department of Materials Science and Engineering, Massachusetts Institute of Technology, 77 Massachusetts Avenue, Cambridge, Massachusetts 02139, United States

Ⓢ *Supporting Information*

ABSTRACT: High-energy irradiation of materials can lead to void formation due to the aggregation of vacancies, reducing the local stress in the system. Studying void formation and its interplay with vacancy clusters in bulk materials at the atomic level has been challenging due to the thick volume of 3D materials, which generally limits high-resolution transmission electron microscopy. The thin nature of 2D materials is ideal for studying fundamental material defects such as dislocations and crack tips and has potential to reveal void formation by vacancy aggregation in detail. Here, using atomic-resolution *in situ* transmission electron microscopy of 2D monolayer MoS$_2$, we capture

rapid thermal diffusion of S vacancies into ultralong (∼60 nm) 1D S vacancy channels that initiate void formation at high vacancy densities. Strong interactions are observed between the 1D channels and void growth, whereby Mo and S atoms are funneled back and forth between the void edge and the crystal surface to enable void enlargement. Preferential void growth up to 100 nm is shown to occur by rapid digestion of 1D S vacancy channels as they make contact. These results reveal the atomistic mechanisms behind void enlargement in 2D materials under intense high-energy irradiation at high temperatures and the existence of ultralong 1D vacancy channels. This knowledge may also help improve the understanding of void formation in other systems such as nuclear materials, where direct visualization is challenging due to 3D bulk volume.
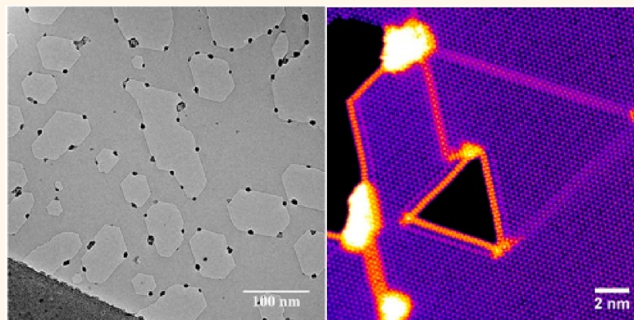
KEYWORDS: voids, vacancies, defects, MoS$_2$, 2D materials, TEM

Structural imperfections in two-dimensional materials influence their electronic, optical, and chemical properties,[1−3] and this has fueled their studies to obtain deeper knowledge. In particular, the focus has been on characterizing both 0D point defects[4,5] and 1D defects such as dislocations,[6] grain boundaries,[7,8] and edges[9] in graphene[10,11] and other 2D materials.[12−14] Monolayer molybdenum disulfide (MoS$_2$) is a direct band gap semiconductor with potential in thin electronic and optoelectronic devices.[15−17] It has been established that S atoms are easier to remove than Mo in MoS$_2$ and that S loss leads to linear defects that alter the band structure, leading to a local semiconducting to metallic transition as the width of the

line defect increases.[18,19] However, upon excessive vacancy density, the stability of materials become compromised, and this is particularly relevant for materials under intense high-energy irradiation, such as materials used in nuclear reactors like graphite.

In general, large numbers of isolated vacancies in materials are energetically unfavorable, and therefore, agglomeration occurs when the energy barrier of migration is overcome,

leading to 3D voids or dislocation loops.[20] This is, in principle, determined by the relative magnitude of the surface and strain energy for each clustered configuration. Surface energy increases for void formation, whereas strain energy increases for dislocation loops. In 2D materials, the edges of holes are similar to the surfaces of 3D voids, and dislocation loops are restricted to 2D. In monolayer hexagonal boron nitride (h-BN), for example, boron monovacancies have been observed to diffuse and coalesce into larger triangular pores, driven by the reduction in surface energy of a larger vacancy that possesses an edge to area ratio lower than that of several isolated small vacancies for the same number of absent atoms.[21] For monolayer graphene, the multivacancy complex for 10 monovacancies has been predicted to be a dislocation pair along a zigzag direction rather than a hole as in h-BN.[22] In this case, the compressional strain field at the ends of the dislocation influence the migration pathway of neighboring monovacancies by reducing the activation barrier.

Prior work in MoS_2 has demonstrated that S vacancies tend to aggregate into a small range linear configurations.[23,24] Dislocations are harder to form because the Mo atoms are difficult to eject from the sample. However, due to the relatively high-energy barrier of S vacancy migration, the reason for the linear arrangement is not clear from either experimental or theoretical studies.[23,25] In this report, we study the details of the formation mechanisms of line defects and voids at the atomic level under conditions where sufficient thermal energy is provided to the system to overcome the diffusion barrier of S vacancies, along with excessive S loss driven by high-energy electron irradiation. An *in situ* heating holder is used to study the behavior at 800 °C and has clean areas of MoS_2, revealing the dynamics without interference from surface contamination.

RESULTS AND DISCUSSION

Ultralong 1D Vacancy Channels. Electron irradiation at room temperature using an accelerating voltage of 60−80 kV typically leads to linear vacancies that are ∼5 nm in length (Figure 1a,b), and the sputtering rate is reduced when amorphous carbon is covering the surface. However, when the sample is heated to 800 °C, the amorphous carbon is removed and the clean MoS_2 surface enables ultralong 1D S vacancy lines up to 70 nm. This is because the S vacancy diffusion is thermally activated and the S point vacancy can rapidly migrate to the low-energy positions (Figure 1c). The linear vacancies at 800 °C are often atomically uniform over 50−70 nm with periodic lattice structure (Figure 1d−f). They occur along the zigzag direction, the same as room temperature, but at high temperature, only a small number of long line vacancies form rather than many smaller line vacancies. The width of the line vacancies at high temperature are mostly 3 S vacancies wide, but in some cases, wider structures can be found. The length of the line vacancy grows with irradiation time (Figure S1).

Annular dark-field scanning transmission electron microscopy (ADF-STEM) is used to deduce the exact atomic configuration of the ultralong 1D vacancies at 800 °C. Two main contrasts are observed, as shown in Figure 2a−f. Using density functional theory (DFT) relaxation of atomic models combined with multislice image simulations and their comparison to the experimental images, we were able to deduce that both of the line defects are similar in composition with two adjacent S vacancy lines in a staggered configuration,
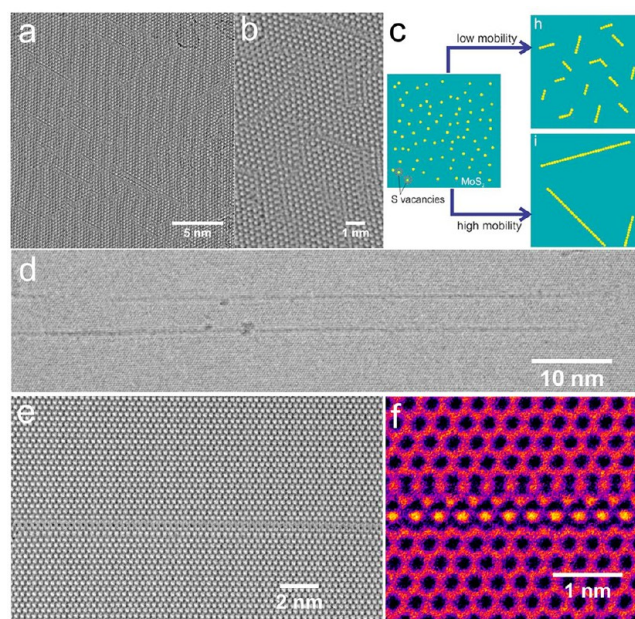
Figure 1. (a) Room temperature phase contrast aberration-corrected transmission electron microscopy (AC-TEM) image of an area of MoS_2 with several short line defects. (b) Higher-magnification image of (a). (c) Schematic diagram showing how S vacancy aggregation into short or long line defects occurs for different mobilities. Low mobility occurs at room temperature, and high mobility occurs at 800 °C. (d) Phase contrast AC-TEM image of MoS_2 at 800 °C, showing contrast features from two ultralong line defects. (e,f) Higher-magnification AC-TEM images at 800 °C of an ultralong line defect in MoS_2, showing uniform atomic periodicity. False color used in (f).

which has been confirmed to be energetically stable.[23] Although these have the same atomic composition, the two types of line defects have different reconstructed configurations, denoted as type I and type II. Magnified images are shown in Figure 2 panel a (type I) and panels f and m (type II). The bright atomic column along the line defect shown in Figure 2f corresponds to a superposition of more than one atom, which is confirmed to be a Mo and a S atom using DFT calculations (Figure 2b−e). The experimental data match the simulated images based on the DFT relaxed models (Figure S2), with only slightly different degrees of out-of-plane distortion (Figure S3a,b). The unit cell for a type I line defect is sufficient to enable curvature along the width of the line, whereas that for a type II line defect possesses a terrace-like configuration. The band structure calculations show a smaller band gap in the line defect region (Figure 2g−l). The presence of two projections of the line vacancies is likely due to influences from nearby line defects that cause some local rippling or strain fields.

DFT calculations were carried out to predict the electronic properties of the line defects. Similar results were obtained for the two types of line defects due to their similar bonding configurations, and therefore, only the results for type II are shown in Figure 2g−l (the results for type I line defect are shown in Figure S4). The two types of line defects were constructed by the same procedure, but with different size of cells (3.17 × 41.40 and 3.17 × 52.63 Å^2, respectively) to represent the possible configurations in various environments. The local bonding character and thus the electronic properties are almost the same for the two configurations, which can be
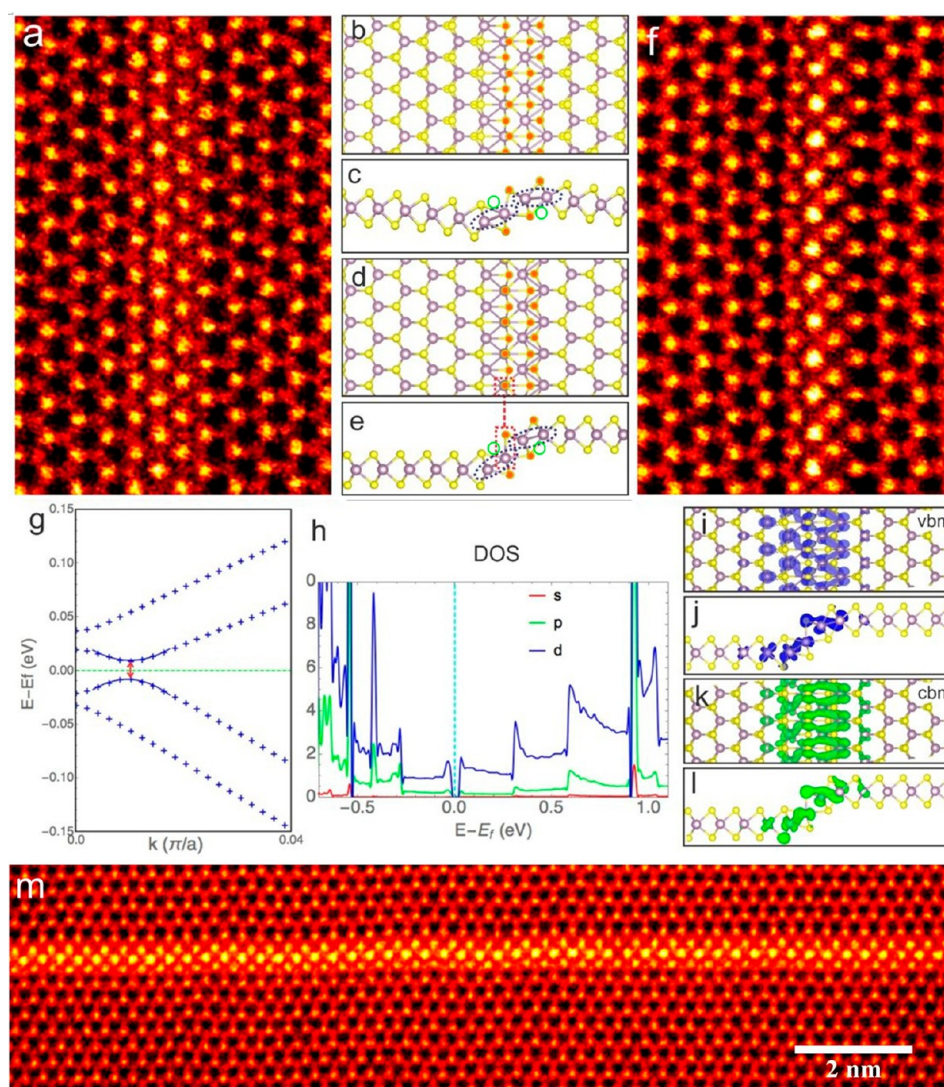
Figure 2. Atomic structures and electronic properties of the extended 2S line defect with two different orientations (type I and type II). Both type I and type II have the similar structure but slightly different orientations and tilting. (a,f) ADF-STEM images of the MoS$_2$ line defect with two different projections observed: (a) type I and (f) type II. (b,d) DFT calculated atomic models corresponding to (a) and (f), with their lateral view shown in (c) and (e). Orange dots indicate single S atoms due to vacancy effects, and green circles indicate the S vacancy sites before reconstruction. (g) Enlarged band structures of type II line defects around the Fermi level, showing the small band gap in the defective structure. Corresponding density of state is shown in (h), with the contribution from each type of orbital separated. (i−l) Wave functions for states around the Fermi level for a type II line defect. (m) ADF-STEM image of a long type II line vacancy.

seen from the slight energy difference (0.063 eV higher for type I compared to type II) and the similar band structures (Figure S5). The models were set to infinity along the line defect length direction to match the long and perfectly periodic line defects observed experimentally. The band-edge dispersion relations for both line defects are parabolic with very small band gaps, 0.019 and 0.017 eV (Figure 2g), 1% of the band gap of the intrinsic monolayer MoS$_2$. The band structures with a broader scope are shown in Figure S5. The orbitals around the Fermi level mainly arise from the d-orbitals of the Mo atoms within and adjacent to the line defects, as shown in Figures 2h and S6. The spin-up and spin-down components are symmetric, indicating zero magnetization for both line defects. The wave functions around the Fermi level (Figure 2i−l) are localized at the line defects, in particular, along the two Mo−Mo bonding chains (highlighted with blue ellipses in Figure 2c,e). This 1D quantum confinement explains the extremely small effective masses for electrons and holes of 0.019 and

0.016 m$_0$, respectively. Importantly, the significant reduction of the band gap and effective mass of the line defects formed at elevated temperatures indicate the possibility of tailoring the band gap of MoS$_2$ by controlled introduction of these line defects.

In order to show that the line defect elongation occurs by the migration of highly mobile S vacancies to a pre-existing line vacancy, we used the spatial control of the electron probe during ADF-STEM imaging to selectively expose a small pristine nanoscale region next to a line defect, as shown in Figure 3. The STEM probe limits the S vacancy production to the small area scanned (the boxed area in Figure 3a); however, extra vacancy lines and elongation of the existing line were produced outside of this area. This confirms that the S vacancies are first generated in the irradiated area and then rapidly migrate to the existing line defect (Figure 3b). After multiple (×10) controlled high-dose scans (30 μs per pixel dwell time) in the white boxed area, we then image the entire
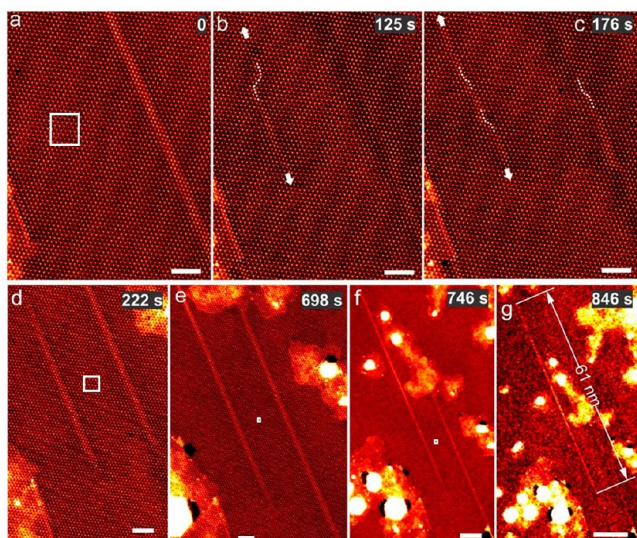
Figure 3. (a−g) ADF-STEM images showing the growth of a line defect from the selected area (white box in (a)). The bright contrast features in (e−f) are metal nanoparticle impurities. Scale bars: (a−e) 2 nm; (f) 5 nm; (g) 10 nm. White boxes show the same area in different frames to help correlate similar regions.

area using a faster scan (16 μs per pixel dwell time) to observe the change in the line defect length (Figure 3g), revealing a long 40 nm line defect that is straight and uniform. At room temperature, electron irradiation causes sub-nanometer pores to be created within the scanned areas instead of ultralong line defects.[26] Long line defects are only created when the diffusion rate of S vacancies is faster than their generation rate (high temperature and clean surface), whereas holes are generated when the diffusion rate is relatively slow compared to that of

the S vacancy generation rate (high dose, room temperature).[26] Short line defects are found when the generation and diffusion rate of S vacancies are comparable, such as when imaging a clean surface at room temperature with defocused illumination.[19]

The growth direction of the line defect (indicated by the white arrows in Figure 3b,c) is along the same zigzag direction as its adjacent line defect, which was already present before the formation of the second one. We observed in many instances that the formation of second ultralong 1D vacancies occurs along the same zigzag direction as the first, indicating that there is some interaction between the two. The formation of the second line defect (left side) in Figure 3a−c affects the first line defect (right side), temporarily resulting in a lattice distortion around the first line defect that causes reduction in the contrast in Figure 3b at the original position of the first line defect. In the initial stage, the line defects showed several kinks, highlighted in Figure 3b,c, which gradually disappear during further growth (Figure 3d−g) as the line vacancy becomes atomically precise in its periodicity. In the last frame (Figure 3g), the created line defect reaches a length of 61 nm. A further example of line defect growth dynamics is shown in Figure S1, where a line defect keeps growing until it encounters a void.

Interactions between line defects and migration of Mo and S atoms are likely to be governed by strain in the system. Strain can be generated in monolayer graphene by intentionally introducing dislocations using a focused electron beam.[27] Unlike the dislocation cores in graphene, which are zero-dimensional and induce "hillock-basin" ripples, a long linear defect will generate a series of wavelike ripples whose wavelength is parallel to the line defect width (one of the armchair orientations). In suspended pristine MoS$_2$, intrinsic ripples have been detected,[28,29] which exhibit a quasi-periodic structure with all ripples being almost parallel and with height
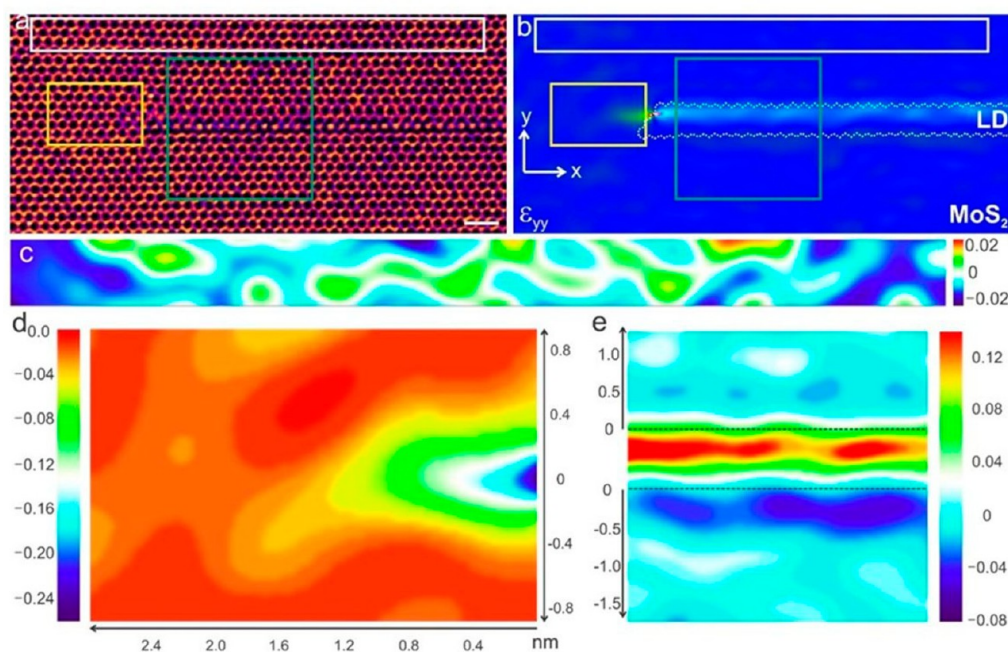
Figure 4. Strain field mapping around a line defect (the same defect shown in Figure 3f). (a) AC-TEM image of a line defect. (b) Corresponding normal strain field along the y direction, with the contour of the line defect indicated by the white zigzag lines. (c) Background strain field in the white box in (a,b), showing the background noise level at $\pm 2\%$. (d) Strain field from the tip of the line defect (yellow box in (a,b)). (e) Strain field within the green box in (a,b), showing an asymmetric strain field along the two sides.
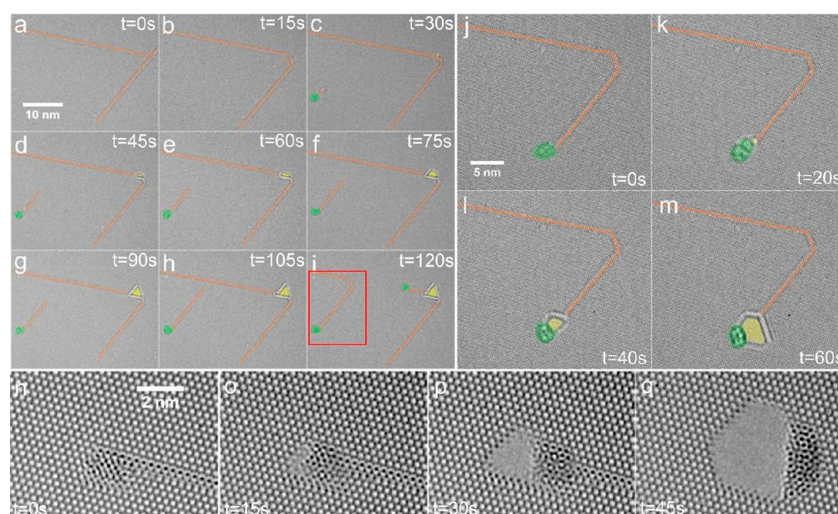
Figure 5. (a−i) Time series of AC-TEM images showing the initial process of void formation from the intersection of nonparallel 1D vacancies. Orange color indicates 1D S vacancy lines; yellow indicates void area, and green indicates surface formed Mo cluster. (j−m) Time series of AC-TEM images of the region indicated by the red box in (i), showing the formation of a void from the Mo nanoparticle region. (n−q) Time series of atomic-resolution AC-TEM images showing the void opening at the tip point of a line defect containing a Mo surface cluster.

variations from several angstroms to tens of nanometers.[28] The parallel ripples result in a periodic compressive strain field, which has been reported to significantly lower the activation energy for the diffusion of monovacancies in graphene.[22] More examples of parallel line defect arrays are shown in Figure S3. The distances between the line defects range from 1 to 30 nm. Nonparallel line defects were also observed in our experiments along the other zigzag directions (Figures 1d and 5a−i), and these are believed to originate from distant locations. However, direct evidence of the rippling nature of the MoS$_2$ lattice cannot be observed as the amplitude of the ripples is not sufficient to induce detectable tilt at a level that can be measured using geometric phase analysis.

Unlike broad line defects with more than three S vacancy lines created at room temperature, the line defects created at elevated temperature are mostly narrow, composed of two S vacancy lines, indicating that the S vacancies prefer to migrate to the tip rather than the side. This behavior can be explained by the strain distributions around the defect. Figure 4a shows a line defect, with its normal strain field in the y direction (ε_{yy}) in Figure 4b. The strain within the line defects at room temperature has been discussed elsewhere, so it will not be included here.[19] A compressive strain field is detected beyond the tip of the line defect (Figure 4d). Within this area, the compressive strain decays from 25 to 4% (the background fluctuation is about ±2%, as shown in Figure 4c, which is most likely induced by out-of-plane distortion arising from the terrace structure). The obvious compressive strain field at the line defect tip can act as a sink for vacancies.[22] Although direct observations are not possible due to the fast migration of S vacancies in comparison to the imaging acquisition time, it is likely that a S vacancy created away from the line defect tip will diffuse randomly until it feels the compressive strain field and then adds to the line defect elongation. The strain field along the sides of the defect area is asymmetric, with one side showing nearly no strain and the other side a compressive strain field ending at the second row of hexagonal rings from the line defect boundary (Figure 4e). The compressive strain field is much lower than that at the outer tip region, in the

range of 4−6%, and is most likely from the in-plane bond length variations and the tilted projection of the lattice due to buckling.

Void/Cluster Formation. After extended electron beam irradiation, the high concentration of S vacancies causes voids to form in the MoS$_2$. The initiation points for the void formation are typically from the intersecting regions of nonparallel 1D ultralong vacancies or the surface-bound Mo clusters at the ends of the 1D line vacancies. Figure 5 shows a sequence of images of intersecting 1D vacancies (Figure 5a), which adjust to a single connected line vacancy with a 60° bend (Figure 5b,c), and then a void begins to open up and grow (Figure 5d−h). In Figure 5i, the void digests the large section of the 1D vacancy to its left, and the remaining section connects to the lower newly formed 1D vacancy with metal Mo nanoparticle at the tip, indicated by the red boxed area in Figure 5i. This tip region is examined in more detail in Figure 5j−m, showing that a void opens up from this Mo nanoparticle area. Figure 5n−q shows a series of aberration-corrected transmission electron microscopy (AC-TEM) images with atomic resolution that captures the void formation process from the Mo nanoparticle cluster that sits at the line vacancy tip. As the void opens up (Figure 5p), the Mo cluster adjusts and binds to the void edge (Figure 5q), and the void grows with zigzag edge terminations. This process is very similar to recent results on Pt nanoparticles on MoS$_2$ monolayers, whereby the Pt etches voids in the MoS$_2$ under electron beam irradiation at high temperature.[30]

Newly formed 1D line vacancies created near pre-existing voids are also digested by the void when they connect, causing void enlargement. Figure 6a−c shows a long S line vacancy within the MoS$_2$, increasing its length until it reaches a pre-existing void (Figure 6d). The line vacancy is then digested by the void, causing its disappearance through the migration of sulfur atoms from the void edge to the line defect region (Figure 6e,f). In Figure 6d, the long line vacancy has just made contact to the void edge, and then in the next frame, it has been digested, and the region where it was in contact with the void now has local sulfur depletion and the creation of small
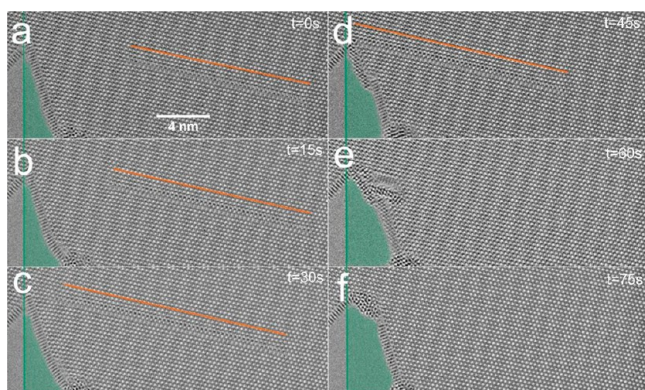
Figure 6. (a−f) Time series of AC-TEM images showing the interaction between a growing S vacancy line and a void. Green shaded area shows the void area change in each frame, and the orange line shows the line vacancy length and position in each frame.

Mo-rich wires. By the next frame in Figure 6f, the wires have transformed into a small Mo cluster, and the void size has enlarged, evident by tracking the green shaded area. This shows that once voids are formed within the MoS_2 monolayer, they can quickly digest large vacancy lines and prevent the formation of new voids in the local area. This is why only a few large voids are created and not many smaller ones. This has the effect to reduce the overall strain energy in the system, where the strain is associated with the bond reconstructions within the 1D line vacancies.

For the void to become enlarged, both Mo and S atoms need to be removed, but Mo sputtering is limited at low accelerating voltages. This causes a buildup of Mo atoms at the void edges that agglomerate into nanocrystals to lower the surface energy of the system. MoS wires also form to terminate the void edges. The line defect connected to a void, shown in Figure 7a,b, enables Mo atoms to migrate along the line defect away from the void edge to the MoS_2 surface, highlighted in white boxes in Figure 7a,b. A preferred position for a single Mo atom on the line defect is observed (5 out of 6 Mo atoms shown in Figure 7a,b adopt this location), which is also predicted from DFT calculations (Figure 7c,d). The binding energy of this configuration is calculated to be 5.7 eV, higher than any other examples we have examined theoretically (Figure S8).

The transport of Mo atoms also occurs when two nonparallel line defects interact during growth, as shown in Figure 7e,f. The two line defects are bridged by an additional short line defect with a wire consisting of consecutive hexagonal motifs with additional Mo atoms (inset to Figure 7a). These are mostly likely to be attracted by the local strain field at the joint position. Later frames (Figure 7g,h) show the formation of Mo clusters when additional Mo atoms are present. The Mo chain also forms when a line defect is linked to a bulk Mo cluster (Figure 7i,j). Image simulations for the atomic models shown in Figure S9 show that this is consistent with two types of hexagonal structures, either with one (white box in Figure 7i) or two (blue box) additional lines of Mo atoms. The bright hexagonal structures are due to a superposition of Mo and S atoms, with a slight distortion as has been observed previously.[31]

In order to understand the migration of Mo atom along a line defect, we performed DFT simulations to explore the
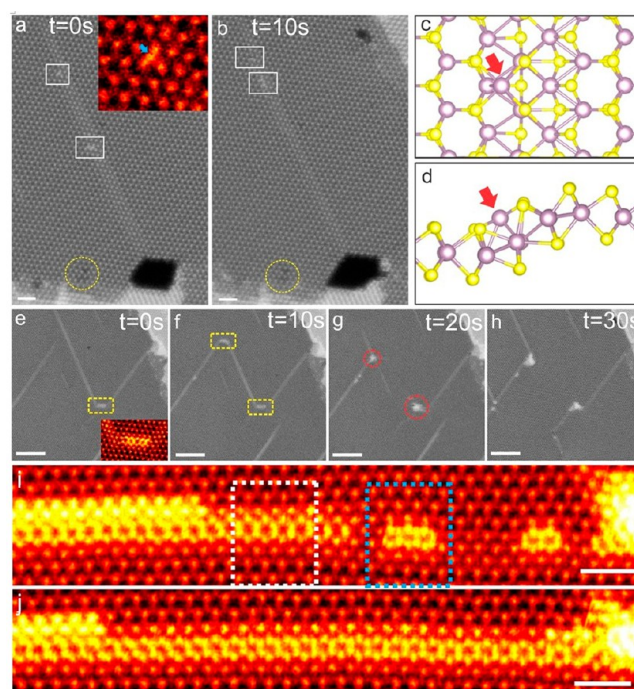
Figure 7. Transport of Mo atoms along line defects. (a,b) ADF-STEM images of several Mo atoms transported through a line defect from a hole, with a magnified image inset. The additional Mo atom is indicated by the blue arrow. (c,d) Atomic model calculated using DFT, showing the energetically favored position of a Mo atom on a line defect. The Mo atom is indicated by the red arrow. (e−h) Series of ADF-STEM images of the interactions between several nonparallel line defects, with the Mo atoms forming short bridges between hexagonal chains (yellow boxes) and clusters at the end of line defects (red circles). (i,j) Two consecutive images, 15 s apart, showing a long, bright chain with additional Mo atom lines on the line defects. The white and blue boxes correspond to Figure S9a,d. Scale bars: (a,b) 1 nm; (e−h) 5 nm; (i,j) 1 nm.

diffusion path connecting energetically favorable structures with the Mo atom bonded to four surrounding S atoms (Figure 8). A $5 \times 1 \times 1$ supercell of the type II line defect was adopted to generate 13 images along the path, with the partial coordinate of Mo atom equally distributed and frozen during the relaxation. As shown in Figure 8g, the hopping barrier for the Mo atom between the most stable configurations (with 5.7 eV binding energy) is 1.6 eV, which is even lower than that of the S vacancy diffusion (2.2 eV). This indicates that the diffusion of the Mo atom along the line defect is quite efficient at high temperature, consistent with our experimental observations. For the reaction path connecting structures with relatively higher energy (5.2 eV binding energy), we obtained a much higher barrier of 3.1 eV (Figure 8h). The large difference in activation energies can be explained by the distinct configurations of the transition states: the Mo atom is embedded in the substrate and connected to the underlying Mo atom for the first path (Figure 8b), while lying on top of the substrate in the bridge configuration for the second path (Figure 8e). The above results suggest that the fast Mo migration is likely to stem from the straight Mo hopping along the line defect assisted by the substrate Mo atoms with low coordination number (each Mo connected with 4 S atoms).

S atom migration also occurs along the 1D vacancy lines, and to understand the migration barriers, we used DFT
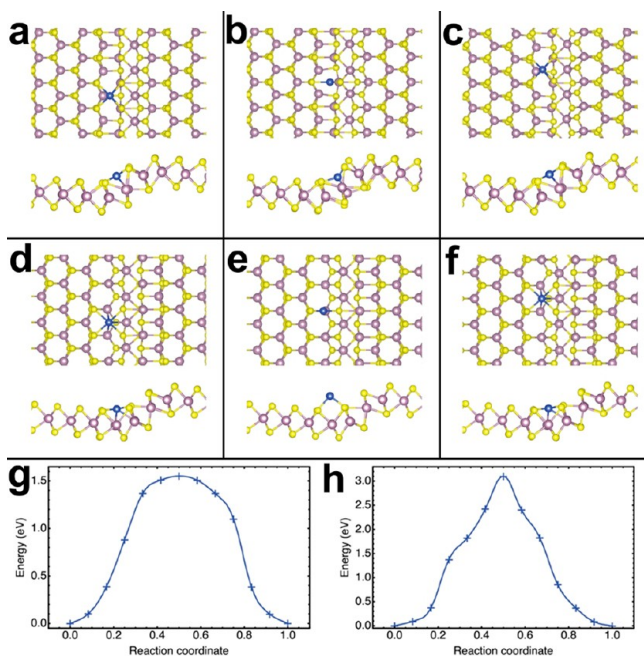
Figure 8. Configurations of the (a,d) initial, (b,e) transition, and (c,f) final states for the reaction paths of the Mo atom (in blue) hopping along the line defects between stable structures with binding energies of (a,c) 5.7 eV and (d,f) 5.2 eV. (g,h) Reaction paths of the Mo atom hopping along the line defects between stable structures with binding energies of (g) 5.7 eV and (h) 5.2 eV.

calculations. As shown in Figure S19, the migration of an on-top S atom proceeds through the bond breaking with one surface S atom and the sequential bond formation with the neighboring S atom along the line defect, resulting in a 1.1 eV hopping barrier (Figure S20). Regarding the S vacancy, migration is accompanied by the variation of coordination number, wherein the transition states have the relevant S atom connecting to only two Mo atoms. The activation energy is estimated to be 0.7 eV (Figure S20). The small diffusion barriers for both paths can be explained by the flexible structure within the line defect, as well as the relatively weak binding of S atom compared to that of the most stable trigonal prismatic configuration. Speculated from its much smaller barrier, S diffusion may proceed much faster than Mo diffusion, and thus Mo migration is likely to serve as the rate-limiting step for the growth of line defects under our experimental

conditions. This is also consistent with the observation that S diffusion is too fast to be captured by our TEM measurement.

In addition to single Mo atoms, Mo clusters are also transported along the line defects at high temperature, as shown in Figure 9. The Mo atoms generated from the void formation migrate along the line defect "highway" to reach the end of the line defect, where a Mo cluster gradually grows on the MoS_2 surface. As expected, the Mo cluster is always at the side of the line defect with compressive strain. The cluster eventually joins a larger Mo crystal that resides on the MoS_2 surface. We also observed that some freely migrating Mo clusters on the MoS_2 surface are present, probably resulting from the detachment of Mo clusters at the line defect ends, and that these can also attach to a preformed 1D S vacancy.

In Figure 10, we discuss the overall processes involved in void formation and its link to the 1D line vacancy growth and digestions. Figure 10a shows that after an hour of electron beam irradiation at high temperatures, massive voids are formed in MoS_2, reaching up to 100 nm in diameter. The MoS_2 material surrounding the void area is still primarily pristine lattice due to the rapid diffusion of vacancies to the voids (Figure 10b). Many large Mo nanocrystal clusters are seen attached to the edges of the voids, with dark contrast in Figure 10b. A significant proportion of the void edges are terminated with MoS wires (Figure 10b,c). By considering the experimental data in the previous figures, we present an overall schematic diagram (Figure 10d−i) that shows the mechanism of void enlargement. When a 1D S vacancy line defect connects to a triangular void (Figure 10d−f), S atoms are removed from the edge region by migrating along the vacancy line and filling empty states. This creates local S depletion at the edge, and the edge reconstructs into MoS wires; at the same time, the 1D S line vacancy shrinks in length as the vacancy sites are filled. Eventually, the 1D S vacancy line is diminished and disconnects from the void (Figure 10g), leaving MoS-terminated void edges. When the 1D S vacancy grows again (Figure 10h) and connects to the void with MoS edge terminations, the Mo-rich edges undergo transformation as more S atoms migrate into the 1D S vacancy channel, and the MoS wires become unstable. MoS wires transform to nanocrystals attached to the void edge, returning the void edge back to normal zigzag lattice termination. Also, some Mo atoms migrate along the 1D S vacancy channel and aggregate at the tip region (Figure 10i), which leads to nanocrystalline Mo clusters on the surface of MoS_2.
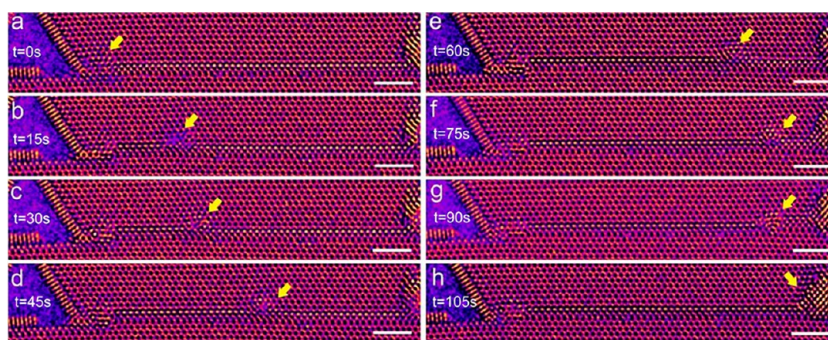
Figure 9. (a−h) Consecutive AC-TEM images showing the migration of a Mo cluster (indicated by yellow arrows) from a hole to the other end of a line defect. Scale bar 2 nm.
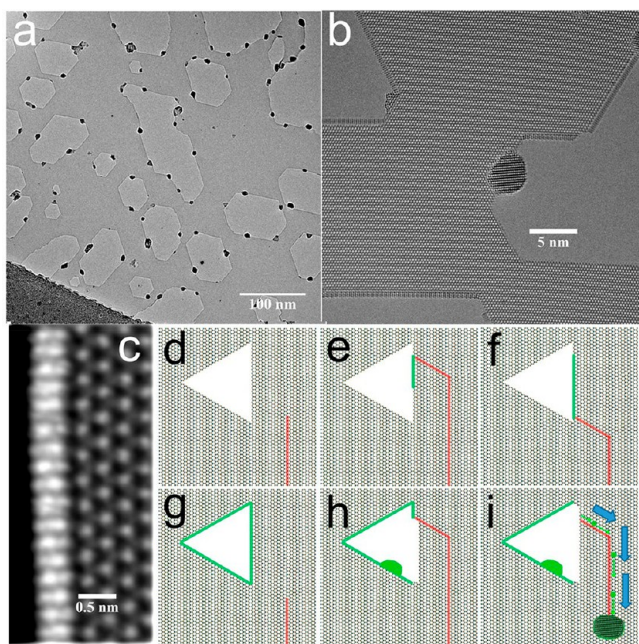
Figure 10. Low-magnification TEM imaging showing the large voids (up to 100 nm) produced in MoS_2 at 800 °C after prolonged electron beam irradiation. The dark contrast from the Mo clusters is also visible. (b) Atomic-resolution AC-TEM image of the sample shown in (a), revealing the pristine lattice, large voids, MoS-wire-terminated edges, and Mo nanoclusters attached to the edges. (c) ADF-STEM image of the MoS wire attached to the zigzag MoS_2 edge. (d−i) Schematic illustration of the void enlargement mechanism. Line defects are indicated by red lines, MoS wires by green lines, and Mo clusters by green. (d) Formed triangular void with a growing 1D S vacancy line (red). (e) 1D S vacancy line (red) has extended and connected to the void with a local region of S depletion at the edge and MoS wire initiation. (f) S atoms from the edge migrate into the 1D S vacancy line, resulting in MoS wire formation at the edge and shortening of the 1D S vacancy line. (g) Large digestion of 1D S vacancy line and the complete termination of void triangle by MoS wires, along with reduction in 1D S vacancy line length. (h) 1D S vacancy line connects to void causing further S depletion, with MoS wire depletion, Mo cluster forming at the edge and void enlargement. (i) Further void enlargement by Mo atom migration along the 1D S line vacancy to the tip point to form Mo surface cluster.

CONCLUSION

We have shown that thermally activated S vacancies created by electron beam irradiation at high temperature can diffuse into ultralong 1D S vacancy line defects along the zigzag lattice directions. The increased density of S vacancies causes the intersection of line vacancies along different zigzag directions that leads to Mo atoms migrating to the surface and the beginning of holes to appear. These small holes grow into large voids with zigzag edge faceting by first the depletion of S at the zigzag edge due to the migration of vacancies to the void edge, which causes the zigzag edge to turn into MoS wires; then as the S vacancy density further increases at the edge, the MoS wires become unstable and they turn into Mo clusters, with the edges back to zigzag termination, and then this process repeats for continual enlargement of the void area. The voids strongly interact with line vacancies, whereby S atoms rapidly diffuse along the vacancy channel from the void edges, and in some cases, the Mo atoms also migrate along these 1D channels. The digestion of line vacancies by voids leads to a small number of

voids that grow larger, which enables the MoS_2 to handle a vacancy concentration before total decomposition higher than that at room temperature. At room temperature, many small voids form and the material rapidly loses mechanical stability and breaks apart. The high defect density at room temperature also corresponds to large strain energy in the system, whereas at high temperature, the void growth enables the reduction in strain energy by the digestion of line vacancies to leave a nearly pristine lattice surrounding the voids. These results reveal some of the most detailed insights into the mechanisms of void formation and its connection to vacancy channels, enabled by the 2D structure of the MoS_2 material.

METHODS

Experimental Methods. *Monolayer MoS_2 Synthesis and Transfer.* The MoS_2 domains were grown on a SiO_2 (300 nm)/Si substrate (University Wafer), which was sonicated in acetone and 2-propanol sequentially, followed by an oxygen plasma treatment. The growth was carried out in a chemical vapor deposition system using 20 mg of MoO_3 powder (99.5%, Sigma-Aldrich) and 500 mg of S (99.5%, Sigma-Aldrich) as the precursor with Ar as the carrier gas under atmospheric pressure. The S powder was placed at the central area of the first furnace in the outer 1 in. quartz tube, whereas the MoO_3 was loaded separately upstream in the second furnace in an inner quartz tube having a smaller diameter of 1 cm. The growth system was first flushed with 500 sccm of Ar gas for 30 min, followed by a preintroduction of S vapor by heating the S powder to ∼180 °C for 10 min under an Ar flow rate of 150 sccm. The second furnace was maintained at 200 °C at the same time to avoid any deposition of solid S on the substrate surface. This ensured that the reaction occurred under a S atmosphere, effectively controlling the initial MoS_2 nucleation density. The second furnace was heated at a rate of 40 °C min^{-1} to 800 °C, whereas the MoO_3 powder reached an approximate maximum temperature of 300 °C. The reaction was conducted at 800 °C for 20 min with 10 sccm Ar. After completion of the reaction, a fast cooling process was applied to quickly stop the growth. A thin film of poly(methyl methacrylate) (PMMA) was then spin-coated on the MoS_2 surface after growth, followed by flotation on 1 mol/L KOH to etch the SiO_2. The PMMA/MoS_2 film was then rinsed by transfer onto deionized water. The rinsed film was subsequently transferred onto a prefabricated *in situ* heating chip and dried in air for 3 h followed by baking at 180 °C for 30 min to increase the adhesion between the MoS_2 and the heating chip. The PMMA was then removed by submerging the heating chip in acetone for 12 h.

Transmission Electron Microscopy with an In Situ Heating Holder. AC-TEM was conducted using Oxford's JEOL JEM-2200MCO TEM operated at 80 kV accelerating voltage with a CEOS imaging aberration corrector. TEM data were recorded using a Gatan Ultrascan 4K × 4K CCD camera with 2 s acquisition times. ADF-STEM was conducted using an aberration-corrected JEOL ARM300CF equipped with a JEOL ETA corrector operated at an accelerating voltage of 60 kV located in the electron Physical Sciences Imaging Centre (ePSIC) at Diamond Light Source. Dwell times of 5−20 μs and a pixel size of 0.006 nm $pixel^{-1}$ were used for imaging with a convergence semiangle of 31.5 mrad, a beam current of 44 pA, and inner−outer acquisition angles of 49.5−198 mrad.

High-temperature imaging up to 800 °C was performed using a commercially available *in situ* heating holder from DENS Solutions (SH30-4M-FS). Heating the sample was achieved by passing a current through a platinum resistive coil imbedded in the TEM chip (DENS Solutions DENS-C-30). The resistance of the platinum coil was monitored in a four-point configuration, and the temperature was calculated using the Callendar−Van Dusen equation (with calibration constants provided by the manufacturer). Slits were fabricated in the Si_3N_4 membranes using focused ion beam milling before being transferred to the MoS_2.

Image Processing and Simulation. ImageJ was used to process the AC-TEM and ADF images. For TEM images, a band-pass filter

(between 100 and 1 pixels) and a Gaussian blur were carefully applied to minimize long-range uneven illumination and reduce noise. For ADF images, only the brightness and contrast of the images were adjusted for visualization. Multislice image simulations for ADF images were performed using the multislice method implemented in the JEMS software with supercells generated from DFT calculations. Parameters for image simulations were based on the experimental condition of the JEOL ARM300CF. The chromatic aberration at 60 kV is 0.89 mm with an energy spread of 0.42 eV. The probe size is 65 pm, and the convergence semiangle is 31.5 mrad. The angle range for dark-field imaging was set from 49.5 to 198 mrad. Spherical aberration was 5 μm.

Density Functional Theory. Standard *ab initio* calculations within the framework of DFT were implemented to explore the structural and electronic properties of ultralong line defects in monolayer MoS_2, using the Vienna Ab Initio Simulation Package (VASP v5.4).[32] Plane-wave and projector-augmented wave-type pseudopotentials were used,[33] with GGA-PBE exchange-correlation functional[34] and a 400 eV kinetic energy cutoff. Dipole correction in the vertical direction was applied to correct the leading errors caused by the slight asymmetry of the surfaces.[35] Spin−orbit coupling effects are taken into account for refinement of electronic structure. The length of the periodic boxes across the type I and type II line defects are 52.6 and 41.4 Å, respectively. A 15 Å vacuum was constructed to eliminate artificial interactions between periodic images. The structures were relaxed until all forces were smaller than 0.02 eV/Å. Monkhorst−Pack k-point grids[5] of $9 \times 1 \times 1$ and $36 \times 1 \times 1$ were used for geometric optimization and electronic structure calculations, respectively.[36] Supercells with the size of $4 \times 1 \times 1$ were generated to obtain the binding energies of Mo atoms on line defects.

ASSOCIATED CONTENT

ⓢ Supporting Information

The Supporting Information is available free of charge on the ACS Publications website at DOI: 10.1021/acsnano.8b01610.

> Propagation rate of line defects, comparison of contrast profiles for ADF-STEM and DFT models; DFT band structures of line defects, strain analysis of line defects, DFT models of Mo atoms on line defect sites, and low-magnification image of large voids (PDF)

AUTHOR INFORMATION

Corresponding Author
*E-mail: jamie.warner@materials.ox.ac.uk.

ORCID ⓘ
Jamie H. Warner: 0000-0002-1271-2019

Author Contributions
¶Q.C. and H.L. contributed equally to this work.

Notes
The authors declare no competing financial interest.

REFERENCES

(1) Han, Y.; Zhou, J.; Dong, J. Electronic and Magnetic Properties of MoS_2 Nanoribbons with Sulfur Line Vacancy Defects. *Appl. Surf. Sci.* **2015**, *346*, 470−476.

(2) Faccio, R.; Mombrú, A. W. The Electronic Structure and Optical Response of Rutile, Anatase and Brookite TiO_2. *J. Phys.: Condens. Matter* **2012**, *24*, 375304.

(3) Topsakal, M.; Aktürk, E.; Sevinçli, H.; Ciraci, S. First-Principles Approach to Monitoring the Band Gap and Magnetic State of a Graphene Nanoribbon *via* its Vacancies. *Phys. Rev. B: Condens. Matter Mater. Phys.* **2008**, *78*, 235435.

(4) Komsa, H.-P.; Kotakoski, J.; Kurasch, S.; Lehtinen, O.; Kaiser, U.; Krasheninnikov, A. V. Two-Dimensional Transition Metal Dichalcogenides under Electron Irradiation: Defect Production and Doping. *Phys. Rev. Lett.* **2012**, *109*, 035503.

(5) Lin, Y.-C.; Bjorkman, T.; Komsa, H.-P.; Teng, P.-Y.; Yeh, C.-H.; Huang, F.-S.; Lin, K.-H.; Jadczak, J.; Huang, Y.-S.; Chiu, P.-W.; Krasheninnikov, A. V.; Suenaga, K. Three-fold Rotational Defects in Two-Dimensional Transition Metal Dichalcogenides. *Nat. Commun.* **2015**, *6*, 6736.

(6) Azizi, A.; Zou, X.; Ercius, P.; Zhang, Z.; Elías, A. L.; Perea-López, N.; Stone, G.; Terrones, M.; Yakobson, B. I.; Alem, N. Dislocation Motion and Grain Boundary Migration in Two-Dimensional Tungsten Disulfide. *Nat. Commun.* **2014**, *5*, 4867.

(7) Barja, S.; Wickenburg, S.; Liu, Z.; Zhang, Y.; Ryu, H.; Ugeda, M. M.; Hussain, Z.; Shen, Z.-X.; Mo, S.; Wong, E.; Salmeron, M. B.; Wang, F.; Crommie, M. F.; Ogletree, D. F.; Neaton, J. B.; Weber-Bargioni, A. Charge Density Wave Order in 1D Mirror Twin Boundaries of Single Layer $MoSe_2$. *Nat. Phys.* **2016**, *12*, 751−756.

(8) van der Zande, A. M.; Huang, P. Y.; Chenet, D. A.; Berkelbach, T. C.; You, Y.; Lee, G.-H.; Heinz, T. F.; Reichman, D. R.; Muller, D. A.; Hone, J. C. Grains and Grain Boundaries in Highly Crystalline Monolayer Molybdenum Disulphide. *Nat. Mater.* **2013**, *12*, 554−561.

(9) Liu, Z.; Suenaga, K.; Wang, Z.; Shi, Z.; Okunishi, E.; Iijima, S. Identification of Active Atomic Defects in a Monolayered Tungsten Disulphide Nanoribbon. *Nat. Commun.* **2011**, *2*, 213.

(10) Lahiri, J.; Lin, Y.; Bozkurt, P.; Oleynik, I. I.; Batzill, M. An Extended Defect in Graphene as a Metallic Wire. *Nat. Nanotechnol.* **2010**, *5*, 326−329.

(11) Botello-Mendez, A. R.; Declerck, X.; Terrones, M.; Terrones, H.; Charlier, J.-C. One-Dimensional Extended Lines of Divacancy Defects in Graphene. *Nanoscale* **2011**, *3*, 2868−2872.

(12) Zhou, W.; Zou, X.; Najmaei, S.; Liu, Z.; Shi, Y.; Kong, J.; Lou, J.; Ajayan, P. M.; Yakobson, B. I.; Idrobo, J. C. Intrinsic Structural Defects in Monolayer Molybdenum Disulfide. *Nano Lett.* **2013**, *13*, 2615−2622.

(13) Liu, Y.; Zou, X.; Yakobson, B. I. Dislocations and Grain Boundaries in Two-Dimensional Boron Nitride. *ACS Nano* **2012**, *6*, 7053−7058.

(14) Enyashin, A. N.; Bar-sadan, M.; Houben, L.; Seifert, G. Line Defects in Molybdenum Disulfide Layers. *J. J. Phys. Chem. C* **2013**, *117*, 10842−10848.

(15) Radisavljevic, B.; Radenovic, a; Brivio, J.; Giacometti, V.; Kis, A. Single Layer MoS_2 Transistors. *Nat. Nanotechnol.* **2011**, *6*, 147−150.

(16) Nourbakhsh, A.; Zubair, A.; Sajjad, R. N.; Tavakkoli K. G., A.; Chen, W.; Fang, S.; Ling, X.; Kong, J.; Dresselhaus, M. S.; Kaxiras, E.; Berggren, K. K.; Antoniadis, D.; Palacios, T. MoS_2 Field Effect Transistors with Sub-10nm Channel Length. *Nano Lett.* **2016**, *16*, 7798−7806.

(17) Liu, Y.; Guo, J.; Wu, Y.-C.; Zhu, E.; Weiss, N. O.; He, Q.; Wu, H.; Cheng, H.-C.; Xu, Y.; Shakir, I.; Huang, Y.; Duan, X. Pushing the Performance Limit of Sub-100nm Molybdenum Disulfide Transistors. *Nano Lett.* **2016**, *16*, 6337−6432.

(18) Ryu, G. H.; Lee, J.; Kim, N. Y.; Lee, Y.; Kim, Y.; Kim, M. J.; Lee, C.; Lee, Z. Line Defect Mediated Formation of Hole and Mo Clusters in Monolayer Molybdenum Disulfide. *2D Mater.* **2016**, *3*, 014002.

(19) Wang, S.; Lee, G.-D.; Lee, S.; Yoon, E.; Warner, J. H. Detailed Atomic Reconstruction of Extended Line Defects in Monolayer MoS_2. *ACS Nano* **2016**, *10*, 5419−5430.

(20) Smallman, R. E.; Bishop, R. J. *Modern Physical Metallurgy and Materials Engineering*, 6th ed.; Butterworth-Heinemann: Oxford, 1999.

(21) Alem, N.; Erni, R.; Kisielowski, C.; Rossell, M. D.; Hartel, P.; Jiang, B.; Gannett, W.; Zettl, A. Vacancy Growth and Migration Dynamics in Atomically Thin Hexagonal Boron Nitride Under Electron Beam Irradiation. *Phys. Status Solidi RRL* **2011**, *5*, 295−297.

(22) Trevethan, T.; Latham, C. D.; Heggie, M. I.; Briddon, P. R.; Rayson, M. J. Vacancy Diffusion and Coalescence in Graphene Directed by Defect Strain Fields. *Nanoscale* **2014**, *6*, 2978−2986.

(23) Komsa, H. P.; Kurasch, S.; Lehtinen, O.; Kaiser, U.; Krasheninnikov, A. V. From Point to Extended Defects in Two-Dimensional MoS$_2$: Evolution of Atomic Structure Under Electron Irradiation. *Phys. Rev. B: Condens. Matter Mater. Phys.* **2013**, *88*, 035301.

(24) Le, D.; Rawal, T. B.; Rahman, T. S. Single-Layer MoS$_2$ with Sulfur Vacancies: Structure and Catalytic Application. *J. Phys. Chem. C* **2014**, *118*, 5346−5351.

(25) Sensoy, M. G.; Vinichenko, D.; Chen, W.; Friend, C. M.; Kaxiras, E. Strain Effects on the Behavior of Isolated and Paired Sulfur Vacancy Defects in Monolayer MoS$_2$. *Phys. Rev. B: Condens. Matter Mater. Phys.* **2017**, *95*, 014106.

(26) Wang, S.; Li, H.; Sawada, H.; Allen, C. S.; Kirkland, A. I.; Grossman, J. C.; Warner, J. H. Atomic Structure and Formation Mechanism of Sub-Nanometer Pores in 2D Monolayer MoS$_2$. *Nanoscale* **2017**, *9*, 6417−6426.

(27) Warner, J. H.; Fan, Y.; Robertson, A. W.; He, K.; Yoon, E.; Lee, G. D. Rippling Graphene at the Nanoscale Through Dislocation Addition. *Nano Lett.* **2013**, *13*, 4937−4944.

(28) Luo, S.; Hao, G.; Fan, Y.; Kou, L.; He, C.; Qi, X.; Tang, C.; Li, J.; Huang, K.; Zhong, J. Formation of Ripples in Atomically Thin MoS$_2$ and Local Strain Engineering of Electrostatic Properties. *Nanotechnology* **2015**, *26*, 105705.

(29) Miro, P.; Ghorbani-Asl, M.; Heine, T. Spontaneous Ripple Formation in MoS$_2$ Monolayers: Electronic Structure and Transport Effects. *Adv. Mater.* **2013**, *25*, 5473−5475.

(30) Wang, S.; Sawada, H.; Chen, Q.; Han, G. G. D.; Allen, C. S.; Kirkland, A. I.; Warner, J. H. *In Situ* Atomic Scale Studies of the Formation of Epitaxial Pt Nanocrystals on Monolayer Molybdenum Disulfide. *ACS Nano* **2017**, *11*, 9057−9067.

(31) Lin, Y.-C.; Dumcenco, D. O.; Huang, Y.-S.; Suenaga, K. Atomistic Mechanisms of the Semiconducting-To-Metallic Phase Transition in Single-Layered MoS$_2$. *Nat. Nanotechnol.* **2014**, *9*, 391−396.

(32) Kresse, G.; Furthmuller, J. Efficient Iterative Schemes for *Ab Initio* Total-Energy Calculations Using a Plane-wave Basis Set. *Phys. Rev. B: Condens. Matter Mater. Phys.* **1996**, *54*, 11169−11186.

(33) Blochl, P. E. Projector Augmented-wave Method. *Phys. Rev. B: Condens. Matter Mater. Phys.* **1994**, *50*, 17953−17979.

(34) Perdew, J. P.; Burke, K.; Ernzerhof, M. Generalized Gradient Approximation Made Simple. *Phys. Rev. Lett.* **1996**, *77*, 3865−3868.

(35) Makov, G.; Payne, M. C. Periodic Boundary-Conditions in *Ab-initio* Calculations. *Phys. Rev. B: Condens. Matter Mater. Phys.* **1995**, *51*, 4014−4022.

(36) Pack, J. D.; Monkhorst, H. J. Special Points for Brillouin-Zone Integrations. *Phys. Rev. B* **1977**, *16*, 1748−1749.